A&A 551, L12 (2013)
DOI: 10.1051/0004-6361/201219854

Astronomy & Astrophysics

Letter to the Editor

Improved mm-wave photometry for kinetic inductance detectors

M. Calvo[1,2], M. Roesch[2], F.-X. Désert[3], A. Monfardini[1], A. Benoit[1], P. Mauskopf[4,7], P. Ade[4], N. Boudou[1], O. Bourrion[5], P. Camus[1], A. Cruciani[1,6], S. Doyle[4], C. Hoffmann[1], S. Leclercq[2], J. F. Macias-Perez[5], N. Ponthieu[3], K. F. Schuster[2], C. Tucker[4], and C. Vescovi[5]

[1] Institut Néel, CNRS & Université Joseph Fourier, BP 166, 38042 Grenoble, France
e-mail: martino.calvo@grenoble.cnrs.fr
[2] Institut de RadioAstronomie Millimétrique, 300 rue de la Piscine, 38406 Saint-Martin d'Hères, France
[3] IPAG, Observatoire de Grenoble, BP 53, 38041 Grenoble, France
[4] Cardiff School of Physics and Astronomy, Cardiff University, CF24 3AA, UK
[5] LPSC, UJF Grenoble 1, CNRS/IN2P3, INPG, 53 rue des Martyrs, 38026 Grenoble Cedex, France
[6] Università di Roma La Sapienza, 00185 Roma, Italy
[7] Dept. of Physics and SESE, Arizona State University, Tempe, Arizona, 85287, USA

Received 3 December 2012 / Accepted 7 February 2013

ABSTRACT

Context. We have developed a dual-band (140 and 220 GHz) mm-wave imaging camera based on superconducting kinetic inductance detector (KID) arrays. Each array contains 132 superconducting resonators whose resonant frequencies are shifted by mm-wave photons absorption. The read out is achieved with a single electronics chain per band, taking advantage of the intrinsic KID frequency-domain multiplexability. The arrays are easily scalable and well adapted for future large format focal plane instruments. NIKA (formerly Néel IRAM KID Array, now New IRAM KID Array) has been specifically designed for the IRAM 30 m telescope at Pico Veleta, and is one of the first instruments using KIDs to have made measurements of astronomical sources.
Aims. In this Letter we describe the solutions adopted to improve the calibration accuracy and the sensitivity of the instrument, and we report on the outcome of the 3rd NIKA observing run of October, 2011.
Methods. We use a fast electronic modulation of the readout tone for each KID pixel in order to linearize the instrument calibration, which we track with measurements of planets. We also adopt a new design of the KIDs, sensitive to both polarizations, to increase the amount of radiation absorbed and thus the optical efficiency of the system.
Results. We measured an average sensitivity on the sky of 21 mJys$^{0.5}$ per beam at 140 GHz and 140 mJys$^{0.5}$ at 220 GHz in the best observing conditions ($\tau_{220} \simeq 0.2$) after atmospheric noise decorrelation. The sensitivity at 220 GHz was limited by the atmospheric attenuation and loading as well as a reduction in the spectral bandwidth due to a misplaced filter. We found the repeatability in the photometry over the entire observing run to be better than 10% in both bands, thus demonstrating a significant improvement over the previous runs. We also find good agreement between NIKA measurements of faint astronomical sources and previous measurements of the same sources.

Key words. instrumentation: detectors – methods: observational – telescopes – techniques: photometric

1. Introduction

Kinetic inductance detectors (KIDs) are superconducting resonators usually fabricated from thin metal films that change their electromagnetic properties in response to incoming radiation. KIDs represent an alternative detector technology to bolometers for future mm and sub-mm large format array instruments. In a bolometer, the incoming optical power is first converted into thermal phonons (heat) in a thermally isolated absorber and the resulting temperature change is measured by a suitable thermometer (Richards 2006). In a KID, on the other hand, incoming photons absorbed by the superconducting film alter the ratio of paired to unpaired charge carriers. This modifies the surface impedance of the superconducting strip which can be parameterized by a complex conductance with an inductive and a resistive component. The change in the so-called kinetic inductance together with the change in residual resistive losses in the superconductor modifies the resonant frequency and quality factor of the KID. A crucial point in favour of KIDs for large format arrays is that they are intrisically suited for frequency domain multiplexing, since the low resistive loss of the superconducting films leads to high resonator quality factors, $Q_{\rm res}$, and therefore high multiplexing ratios (Day et al. 2003).

The New IRAM KID Array (NIKA) is a dual-band imaging camera operating at frequencies of 140 and 220 GHz with 132 KID pixels per band. In the first two observing runs at the IRAM 30 m telescope NIKA demonstrated sensitivities within a factor two of state-of-the-art instruments based on well-established bolometers technology (Monfardini et al. 2010, 2011). However, in these runs NIKA was not able to measure the brightness of sources with good repeatability from pixel to pixel due to the large changes in responsivity of the KIDs under changes in optical loading. In the next section we describe an innovative modulated readout scheme which enables the optical power absorbed by a KID to be continuously monitored and leads to a large improvement in the consistency of the photometric calibration. In Sect. 3 we present the new dual-polarization KID design adopted. In Sect. 4, we show results obtained during the third NIKA observing run (October, 2011). Variable weather during the run allowed us to test the performance of the KIDs in a broad range of conditions.

2. Modulated readout for kinetic inductance detectors

The resonant frequency, f_0, of a KID is determined by the geometry of the resonator and the surface impedance of the superconducting film. In NIKA the KID resonant frequencies are from 1−1.5 GHz. Because the surface impedance is sensitive to variations in the density of superconducting carriers, photons with high enough energy to break apart superconducting Cooper pairs will induce a shift in the resonant frequency. For thin films, the relationship between the shift, δf_0, of the resonant frequency and the incoming optical power, $P_{\rm opt}$, is linear for small variations in $P_{\rm opt}$ (Swenson et al. 2010).

Each KID is weakly coupled to a nearby microwave transmission line which carries a readout tone signal close to the resonant frequency of every detector in an array. The amplitude and phase of each transmitted and reflected signal is affected by the corresponding KID. Near resonance the ratio of the transmitted signal to the input signal is given by:

$$S_{21}(f) = 1 - \frac{Q_{\rm res}}{Q_{\rm c}} \frac{1}{1 + 2{\rm i}\, Q_{\rm res}(f - f_0)/f_0} \quad (1)$$

where $Q_{\rm c}$ is the coupling quality factor (Zmuidzinas 2012). It is possible to reconstruct the changes in $S_{21}(t)$, and thus in $f_0(t)$, by monitoring the time-varying in-phase (I(t)) and in quadrature (Q(t)) components of the transmitted signal corresponding to a given input tone signal sent into the cryostat, as I and Q are directly related to the real and imaginary components of S_{21}.

The multiplexing electronics used for the KID readout is described in Bourrion et al. (2011), and is based around an FPGA which synthesizes a bias signal containing a set of tone frequencies in the range of 0−250 MHz that are used to excite each of the resonators in an array. These tones are up and down converted by mixing them with a local oscillator carrier signal (LO) of frequency $f_{\rm LO}$ ($f_{\rm LO}$ = 1.312 GHz in our setup).

One of the challenges of operating a KID compared to a device with a dissipative readout like a bolometer is converting the observed ($I(t)$, $Q(t)$) values to an absorbed optical power or shift in resonant frequency as a function of time, $\delta f_0(t) \propto \delta P_{\rm opt}(t)$. In the previous NIKA observing runs this was accomplished by making a frequency sweep before starting a scan, roughly every few minutes. For each detector it was then possible to determine the center of the resonance circle and the phase $\phi(f)$ of a point in the (I, Q) plane as a function of frequency. Assuming that the change in phase for a shift in the resonant frequency is linear for small variations of ϕ this can be used to estimate $\delta f_0 = \frac{\delta\phi}{{\rm d}\phi/{\rm d}f}$. If a resonance is not perfectly symmetric then the factor, $\frac{{\rm d}\phi}{{\rm d}f}$ is not constant for fairly small changes in $P_{\rm opt}$. In principle this can be corrected using the details of the shape of each resonant feature.

However, in practice, this approach led to poor photometric reproducibility of approximately 30%.

To address this problem we have developed a system to constantly monitor the rate of change of the signal, $\left(\frac{{\rm d}I}{{\rm d}f}, \frac{{\rm d}Q}{{\rm d}f}\right)$ using a known frequency shift, that we *artificially* create by modulating the frequency of the LO by a fixed quantity, $\delta f_{\rm LO}$ ($\delta f_{\rm LO}$ = 2 kHz in our case). The LO frequency is modulated synchronously to the FPGA data acquisition rate at about 1 kHz, so that the values of (I, Q) sampled by the FPGA correspond to frequencies alternating between $f^i_+ = f^i_0 + \delta f_{\rm LO}/2$ and at $f^i_- = f^i_0 - \delta f_{\rm LO}/2$. The time ordered data values $(I(t), Q(t))_i$ from detector i are given by:

$$(I(t), Q(t))_i = \left(\frac{I(f^i_+) + I(f^i_-)}{2}, \frac{Q(f^i_+) + Q(f^i_-)}{2}\right) \quad (2)$$

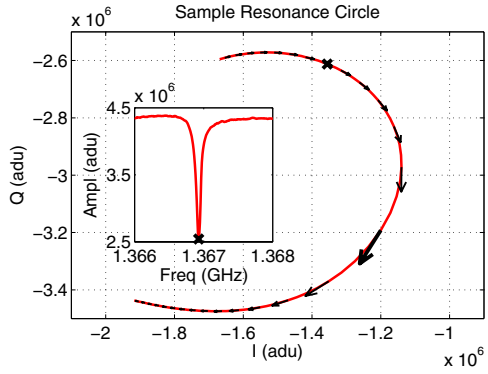

Fig. 1. Typical KID resonance circle in raw A/D units at the input of the FPGA. The line (red online) represents the (I, Q) data of the frequency sweep around the resonance, and the arrows are the $\left(\frac{{\rm d}I}{{\rm d}f}, \frac{{\rm d}Q}{{\rm d}f}\right)$ measured for a 2 kHz modulation of the LO. The largest arrow corresponds to the frequency where the amplitude of the $\left(\frac{{\rm d}I}{{\rm d}f}, \frac{{\rm d}Q}{{\rm d}f}\right)$ vector is the largest: this is the frequency used to read out the detector.

and the corresponding differential values are:

$$\left(\frac{{\rm d}I}{{\rm d}f}(t), \frac{{\rm d}Q}{{\rm d}f}(t)\right)_i = \left(\frac{I(f^i_+) - I(f^i_-)}{\delta f_{\rm LO}}, \frac{Q(f^i_+) - Q(f^i_-)}{\delta f_{\rm LO}}\right). \quad (3)$$

A preliminary sweep around the resonance, such as the one in Fig. 1, is still necessary in order to correctly place the excitation tones, but is not required for calibration. During a scan, the value of δf_0 for each pixel, i, is obtained comparing the difference $(\Delta I(t), \Delta Q(t))_i$ between successive $(I(t), Q(t))_i$ points with the gradient $\left(\frac{{\rm d}I}{{\rm d}f}(t), \frac{{\rm d}Q}{{\rm d}f}(t)\right)_i$ used as a reference. This is achieved by projecting $(\Delta I(t), \Delta Q(t))_i$ along the gradient itself.

The total frequency shift of a resonator between times t_1 and t_2 is $\Delta f_0(t_2 - t_1)$ which is proportional to the difference in the absorbed power $\Delta P(t_2 - t_1)$ and is given by the integral of $\delta f_0(t)$ from t_1 to t_2. Using this scheme, as the observing conditions vary, the coefficient linking $(\Delta I, \Delta Q)$ to δf_0 is automatically updated, making the measurements much less sensitive to background fluctuations.

This method of determining absorbed optical power in a KID is simple and convenient but still affected by some systematic uncertainty. Indeed, the instantaneous differential value $\left(\frac{{\rm d}I}{{\rm d}f}, \frac{{\rm d}Q}{{\rm d}f}\right)$ is calculated by modulating the LO frequency, and is therefore tangent to the (I, Q) circle for a *fixed* background optical power (see Fig. 1). On the other hand, the actual variation $(\Delta I, \Delta Q)$ occurs for a fixed excitation frequency and is due to a difference in the optical power, which includes a change in the (I, Q) circle radius. This is physically related to the fact that an increase in the quasiparticle density leads to a larger kinetic inductance value as well as more loss in the superconductor. The observed (I, Q) trajectory is therefore not exactly parallel to the direction given by $\left(\frac{{\rm d}I}{{\rm d}f}, \frac{{\rm d}Q}{{\rm d}f}\right)$, but typically different by less than 10°, so that the estimated error introduced by the projection method is less than 2% for faint sources.

For bright sources such as Mars the change in optical load can shift the resonances far from their excitation frequency, and lead to distortions in the (I, Q) plane. To address this we assume a polynomial relationship between the (I, Q) point and the frequency f of the form

$$f(I, Q) = \sum_{i+j \le n} a_{ij} I^i Q^j. \quad (4)$$

From this formula, it is possible to evaluate the expected variation of (I, Q) for a known variation of f, and then to fit the

a_{ij} coefficients so as to make the theoretical values and the observed $\left(\frac{dI}{df}, \frac{dQ}{df}\right)$ values match over a scan. Once the a_{ij} are determined by matrix inversion this method yields a relation between the observed (I, Q) values and the resonant frequency of each pixel. For $n = 3$, the value of $\Delta f_0(t_2 - t_1)$ given by the projection method and the one found using the polynomial approach is almost identical in all but the extreme situations (i.e. very strong sources). In this case Δf_0 can be calculated only after the end of the scan, and we find consistently higher values of absorbed power with the polynomial fit than with the simple projection.

3. Dual-polarization detectors design

A lumped element KID (Doyle et al. 2008) is a planar resonator which consists of an interdigital capacitor and a meandering inductor shaped to directly absorb the incoming radiation. The classical design (Monfardini et al. 2010) is only sensitive to radiation polarized parallel to the main lines of the inductor. For a purely imaging experiment, like NIKA, this results in reduced overall quantum efficiency. We therefore adopted a new design, in which the inductance is based on a Hilbert curve of 3rd order (Roesch et al. 2012). This fractal pattern can absorb both polarizations. To take full advantage of the new design, we replaced the grid polarizer splitter used in previous runs with a 45° dichroic. This allows to effectively double the optical efficiency of the 140 GHz band, which is now around 30%. The improvement was lower at 220 GHz as a consequence of a misplaced filter in the optical chain. The filters used had an effective transmission band of 200−240 GHz, whereas the atmospheric window of interest is 200−280 GHz. For a thermal continuum spectrum, that translates in a loss of over 50% of the available optical power, without affecting the performances of the readout chain, which is the main noise source. The resulting sensitivity is thus degraded by more than a factor two. The noise spectrum of the detectors, after sky-noise subtraction, is relatively flat down to 0.1 Hz in good weather conditions.

We adopted the same geometry for both arrays, each consisting of 132 pixels with a pitch of 2.3 mm, giving an effective focal plane sampling of approximately $0.75F\lambda$ at 140 GHz and $1.25F\lambda$ at 220 GHz. Out of the 132 pixels, we found 103 (116) valid resonances for the 140 GHz (220 GHz) band. Taking out the 12 (12) overlapping resonances and the 24 (15) showing instable or doubtful behaviour, we have a total of 67 (89) valid pixels, in the two bands.

4. Results

To show the effectiveness of the improved calibration technique we present results from a small set of primary and secondary calibrators. For this analysis we rely on the polynomial fitting approach to estimate the observed frequency shift.

As a primary calibrator we use Mars, assumed to be a 202 K blackbody source which during the run had a diameter of 5.6 arcsec. To span the whole array, the typical map size is about 6 arcmin wide. The point-source flux is then obtained with a fixed-width Gaussian fitting technique with a full width at half maximum of 18 arcsec (16 arcsec) for the 140 GHz (220 GHz) channels respectively. To be able to compare results from different maps, we used the same approach to reduce the data on other sources like Uranus, Neptune and the Galactic source MWC349, used as secondary calibrators. We first use a map of Mars to extract the response of each KID to a known source (primary calibrator). This gives us a Hz/Jy conversion factor per detector. Then we make a map of a secondary calibrator, and measure the flux we observe on each KID using the conversion factor we found. The dispersion of the fluxes from pixel to pixel around the mean value gives us a measure of the repeatability of the calibration.

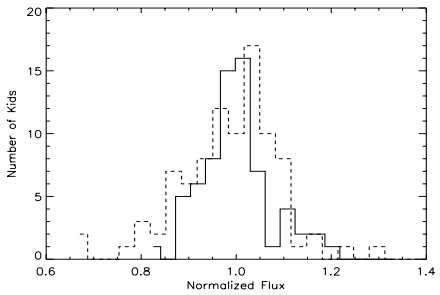

Fig. 2. Histogram of the normalized signals observed on Uranus with the arrays at 140 GHz (full line) and 220 GHz (dashed line).

Figure 2 shows the normalized distribution of calibrated flux for all of the useful KIDs of the two channels from one observation of Uranus. The dispersion among the valid detectors around the mean value is 7% (9%) for the 140 GHz (220 GHz) channels. While the signal-to-noise ratio of each measurement by individual pixels is much larger than 100, some of the dispersion in a single measurement can be attributed to variations in sky opacity during a scan, variations in the baseline due to filtering or common mode subtraction of sky noise, and variations in the beam shapes due to focus or pointing errors. Overall, we find a good consistency between the flux measured by the valid detectors, especially if we consider that the observations of Mars and Uranus were performed 10 h apart, that the background was different, and that we retuned the excitation tones many times between the two maps. Similar results have been obtained with all the secondary calibrators used. The repeatability of the photometry achieved with the new method allows now, for the first time, deeper integrations.

We correct for the attenuation of the astronomical sources due to non-zero atmospheric opacity, τ, by correlating this with the average resonant frequencies of the detectors. As the atmosphere becomes more opaque, its emission also increases leading to an increase in the background load and lowering the resonant frequencies of the KIDs. It is therefore possible to find a function $\tau(\langle f_0^i \rangle)$ by relating the average resonance position $\langle f_0^i \rangle$ to the external measurement of τ read by a tipping 225 GHz taumeter. Through this function we are able to extrapolate the atmospheric opacity during a scan with an uncertainty of <10%.

We compare the flux measured by NIKA from 8 bright millimetre quasars with that obtained by the Plateau de Bure interferometer. The 140 GHz NIKA fluxes are on average 93% the PdB fluxes, within the 10% absolute uncertainty of PdB data.

To estimate the sensitivity of our arrays we also observed several faint point sources. Here we show the measurements of 4C05.19 (MG J0414+0534) and APM08279+5255. The data are binned in sky coordinates after a sky-noise decorrelation procedure based on a common-mode linear subtraction.

4C05.19 is a gravitationally lensed quasar at a redshift of 2.64. We made 7 consecutive on-the-fly maps of the source during a ∼1500 s observation with a zenith opacity of 0.09 at 140 GHz. Because the size of the scan was larger than the array size, the on-source integration time was approximately 700 s. From the 140 GHz map in Fig. 3 we measure a flux of 27.1 ± 1.4 mJy. This value is consistent with the measurements at longer and shorter wavelengths reported in literature (Fig. 4). At 220 GHz we get a marginal detection with a flux of 23±9 mJy.

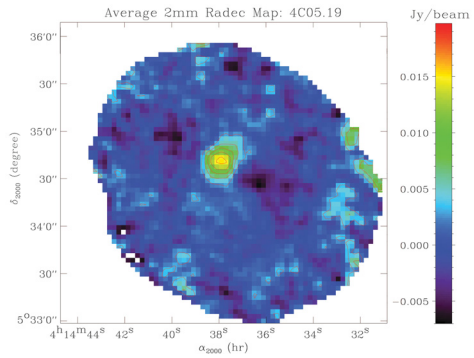

Fig. 3. Map of quasar 4C05.19 at 140 GHz. The data have been smoothed with a 5 arcsec Gaussian filter.

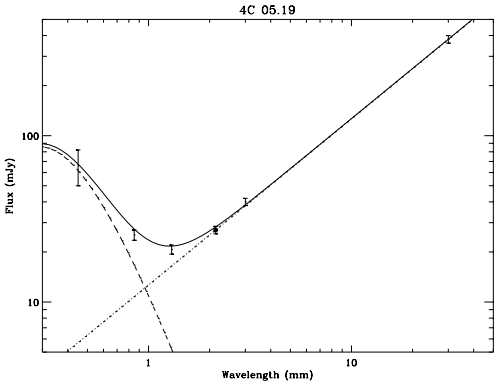

Fig. 4. (sub)mm spectrum of the quasar 4C05.19. The black circle is the value obtained here in the third NIKA run, whereas other data are taken from Barvainis & Ivison (2002) and Kellermann & Pauliny-Toth (1973). Absolute photometric uncertainties have not been included. The spectral energy distribution fit includes a power-law synchrotron component (dotted line) and a contribution from dust emission (dashed line).

APM08279+5255 is another gravitationally lensed quasar at a redshift of 3.91. Its spectral energy distribution is shown in Fig. 5. The measured 140 GHz flux of 6.6 ± 1.3 mJy was obtained in a 3000 s observation with a zenith opacity of 0.11 at 140 GHz and an on-source integration time of ≃1000 s. The flux of 17 ± 7 mJy observed at 220 GHz is less precise compared to previous measurements. As in the case of 4C05.19, however, it is compatible with literature data.

Accounting for the effective time spent by all detectors on the source, the noise equivalent flux density (NEFD) measured in several blank sky observations averaged over the array is 21 mJy $s^{0.5}$ per beam at 140 GHz and 140 mJy $s^{0.5}$ per beam at 220 GHz. These figures have been obtained in the best opacity conditions experienced during the run (τ_{220} = 0.2, stable atmosphere). On the other hand, the observations presented previously have been carried out in average weather. This explains the reduced effective sensitivity, in particular for the 220 GHz band, more affected by the atmospheric absorption and sky noise.

5. Conclusions and perspectives

We have developed a modulated readout scheme that allows continuous simultaneous tracking of multiple KID resonant frequencies which change proportionally to the absorbed optical power. With this readout, we demonstrate photometric reproducibility

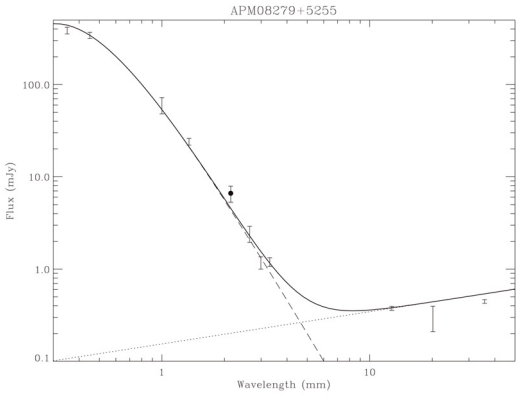

Fig. 5. (sub)mm spectrum of the quasar APM08279+5255. The black circle is the value obtained here in the third NIKA run, whereas other data are taken from Beelen et al. (2006), Garcia-Burillo et al. (2006), Wagg et al. (2006), Krips et al. (2007) and Riechers et al. (2009). The spectral energy distribution model by Beelen et al. (2006) is shown as the black line. It includes a dust component (dashed line) and a synchrotron component (dotted line).

with the NIKA instrument of around 7% and 9% for the 140 GHz and 220 GHz channel respectively. A first attempt at using total power as a measurement of opacity gives an absolute photometric accuracy of about 10%. To further reduce the systematic uncertainty to the level of 2% required by the next generation instruments an additional internal optical calibrator is being designed for the larger field-of-view (6.5 arcmin) NIKA2 camera.

In addition, we demonstrate an improved sensitivity of the KID arrays: a conservative estimate of the NEFDs is 21 mJy $s^{0.5}$ per beam at 140 GHz and 140 mJy $s^{0.5}$ per beam at 220 GHz. A misplaced filter and poor weather conditions partially explain the 220 GHz figure. Laboratory measurements on newly designed 220 GHz arrays have shown highly encouraging results.

NIKA is now permanently installed at the Pico Veleta telescope, and will remain on site until 2014, when it will be replaced by the new NIKA2 kilopixel instrument.

Acknowledgements. We thank Santiago Navarro, Juan Peñalvez, Carsten Kramer and the whole IRAM staff for the outstanding support during the preparation, installation and the observations. Part of this work was supported by the French National Research Agency Grant No. ANR-09-JCJC-0021-01 and by the STFC Bridging Grant No. ST/J001449/1.

References

Barvainis, R., & Ivison, R. 2002, ApJ, 571, 712
Beelen, A., Cox, P., Benford, D. J., et al. 2006, ApJ, 642, 694
Bourrion, O., Bideaud, A., Benoit, A., et al. 2011, JINST, 6, P06012
Day, P. K., Leduc, H. G., Mazin, B. A. et al. 2003, Nature, 425, 817
Doyle, S., Mauskopf, P., Naylon, J., et al. 2008, J. Low Temp. Phys., 151, 530
Garcia-Burillo, S., Gracia-Carpio, J., Guelin, M., et al. 2006, ApJ, 645, L17
Kellermann, K. I., & Pauliny-Toth, I. I. K. 1973, AJ, 78, 828
Krips, M., Peck, A. B., Sakamoto, G. B., et al. 2007, ApJ, 671, L5
Mazin, B. 2004, Ph.D. Thesis, California Institute of Technology, USA
Monfardini, A., Swenson, L. J., Bideaud, A., et al. 2010, A&A, 521, A29
Monfardini, A., Benoit, A., Bideaud, A., et al. 2011, ApJ, 194, 24
Richards, P. L. 1994, J. Appl. Phys., 76, 1
Riechers, D., Walter, F., Carilli, C. L., & Lewis, G. F. 2009, ApJ, 690, 463
Roesch, M., Benoit, A., Bideand, A., et al. 2011, Proc. of the ISSTT2011 workshop [arXiv:1212.4585]
Swenson, L. J., Cruciani, A., Benoit, A., et al. 2010, APL, 96, 263511
Wagg, J., Wilner, D. J., Neri, R., et al. 2006, ApJ, 651, 46
Yorke, H. W. 1980, A&A, 86, 286
Zmuidzinas, J. 2012, Annu. Rev. Cond. Mat. Phys., 3, 169